

SECONDARY MOTION IN TURBULENT FLOWS OVER SUPERHYDROPHOBIC SURFACES

Yosuke Hasegawa

Institute of Industrial Science
The University of Tokyo
Komaba 4-6-1, Meguro-ku, Tokyo 153-8505, Japan
ysk@iis.u-tokyo.ac.jp

Sebastian Tuerk

Graduate School of Computational Engineering
Numerical Methods in Mechanical Engineering
Technical University of Darmstadt
Dolivostr. 15, 64293 Darmstadt, Germany
tuerk@fnb.tu-darmstadt.de

Alexander Stroh, Getraud Daschiel, Bettina Frohnappel

Institute of Fluid Mechanics
Karlsruhe Institute of Technology
Kaiserstr. 10, 76131 Karlsruhe, Germany
alexander.stroh@kit.edu, gertraud.daschiel@kit.edu, bettina.frohnappel@kit.edu

ABSTRACT

We investigate the effects of superhydrophobic surface carrying streamwise micro grooves on the flow dynamics and the resultant gain in the flow rate in a fully developed turbulent channel flow under a constant pressure gradient. The superhydrophobic surface is modeled as a flat boundary with alternating no-slip and slip conditions, and a series of direct numerical simulations is performed with systematically changing the spanwise periodicity of the streamwise grooves. It is observed that the alternating no-slip and slip boundary conditions cause a spanwise inhomogeneity of the Reynolds shear stress near the superhydrophobic surface, and consequently generate Prandtl's second kind of secondary flow characterized by coherent streamwise vortices. Accordingly, the instantaneous turbulent flow is decomposed into the spatial-mean, coherent and random components. The detailed turbulent statistics of the three components are obtained and the effect of the secondary flow on the resultant drag reduction is discussed.

INTRODUCTION

The reduction of skin friction drag in turbulent flows is an important issue in efficient use of available energy resources. One interesting option for water flows in this respect is the use of superhydrophobic surfaces. These surfaces consist of a thin-film hydrophobic coating with a certain roughness pattern. Air bubbles that are entrapped in the cavities of the roughness pattern can locally provide slip-like properties. This results in a significant reduction of the skin friction drag compared to a smooth and fully wetted water-solid interface.

Philip (1972) modeled the superhydrophobic surface as an alternating boundary condition between no-slip and free-slip using the Navier boundary condition for solid-fluid interfaces on microscopic scale. By averaging over the entire

surface, an average slip velocity at the wall, u_s , is obtained:

$$u_s = l_s \left(\frac{\partial u}{\partial y} \right)_w \quad (1)$$

where l_s denotes the effective slip length relating the slip velocity and the velocity gradient at the wall (subscript w). For Stokes flow through a two-dimensional channel with a superhydrophobic roughness pattern consisting of longitudinal or transversal grooves, Philip (1972) derived analytical solutions of the slip velocity and the resultant drag reduction: the effective slip length over streamwise grooves is exactly twice as large as that over transverse ones.

Considering that most engineering flows are turbulent such that the friction drag is significantly increased compared to laminar flows, the potential application of a superhydrophobic surface to turbulent flow for drag reducing purposes is of great interest. First experiments by Daniello et al. (2009) have demonstrated that the superhydrophobic surface turns out to be quite promising in the turbulent regime. They found significant drag reduction with a slip length much smaller than the channel height. In laminar flows, on the contrary, the effective slip length has to be of the same order of magnitude as the channel height to achieve a significant drag reduction rate.

In order to analyze the properties of a turbulent flow field above superhydrophobic surfaces we carry out direct numerical simulations (DNS) of turbulent channel flows where the superhydrophobicity on top and bottom walls are modeled by alternating local free-slip and no-slip boundary conditions which resemble the boundary conditions of a surface structure with air-filled grooves in streamwise direction. In previous studies superhydrophobic surfaces have often been represented with a uniform slip length over a flat fluid-solid boundary (Min et al. 2004, Fukagata et al. 2006)

This assumption is valid only when the typical length-scale of the surface structure is sufficiently smaller than

that of near-wall turbulence. With the introduction of spatially varying boundary conditions, we observe significant inhomogeneity of the Reynolds shear stresses near a superhydrophobic surface. This results in the Prandtl's second kind of secondary flow. This phenomenon cannot be reproduced by the conventional uniform slip length approach, and has not been reported in previous simulation where alternating no-slip/free-slip boundary conditions are employed (Martell et al., 2009).

NUMERICAL PROCEDURE

We carry out direct numerical simulations of a fully developed channel flow under a constant pressure gradient with the friction Reynolds number set at $Re_\tau = u_\tau \delta / \nu = 180$, where u_τ , δ and ν are the friction velocity, the channel half depth height and the kinematic viscosity of the fluid, respectively. The applied boundary conditions and the computational domain are illustrated in figure 1, where x , y and z correspond to the streamwise, wall-normal and spanwise directions, respectively. The flow is bounded by alternating no-slip free-slip boundary conditions on the bottom ($y = 0$) and top wall ($y = 2\delta$), while periodic boundary conditions are applied in the streamwise and spanwise directions.

For an incompressible Newtonian fluid, the flow has to satisfy the continuity and Navier-Stokes equations in the following form:

$$\frac{\partial u_i^*}{\partial x_i^*} = 0. \quad (2)$$

$$\rho^* \frac{Du_i^*}{Dt^*} = -\frac{\partial p^*}{\partial x_i^*} + \mu^* \frac{\partial^2 u_i^*}{\partial x_j^{*2}}. \quad (3)$$

where p^* is the static pressure and μ^* is the dynamic viscosity. Throughout this paper, the asterisk denotes a dimensional quantity. Otherwise quantities are non-dimensionalized by the friction velocity, u_τ^* , and the kinematic viscosity, ν^* , such that $u = u^*/u_\tau^*$ and $x_i = x_i^* u_\tau^*/\nu^*$ (wall units). Note that, as the pressure gradient is kept constant during the simulation, u_τ^* and Re_τ are constant consequently. By doing so, the gain due to a superhydrophobic surface is measured in terms of an increase in flow rate compared to a turbulent channel flow with purely no-slip walls at top and bottom. This approach is chosen since the alternative setup in which a constant flow rate is prescribed will lead to very low friction Reynolds numbers for the large drag reduction that is expected with superhydrophobic surfaces (Busse and Sandham, 2012). Potential changes in the turbulence properties due the presence of superhydrophobic surfaces might be masked through this Reynolds number effect.

As numerical scheme, a fractional step method on a staggered grid is used. For spatial discretization a second-order finite difference method is used while for temporal discretization, the second order Adams-Bashforth method is applied for the convection terms and the Crank-Nicolson method is applied for the viscous terms.

The number of grid points employed is $(N_x, N_y, N_z) = (128, 129, 256)$ and the domain width is set to $(L_x^*, L_z^*) = (2.5\pi\delta^*, \pi\delta^*)$ in all present cases. This results in the grid

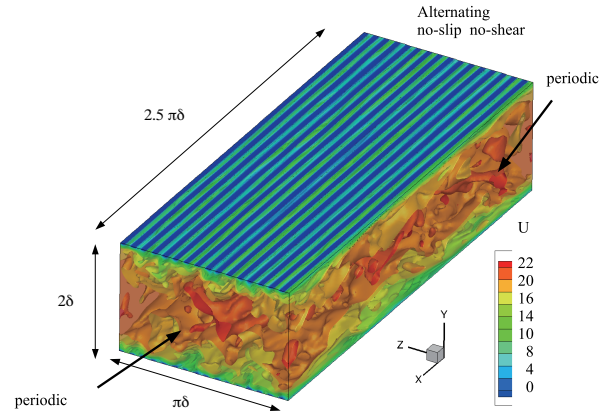


Figure 1. Illustration of the computational domain and the instantaneous velocity field, including applied boundary conditions

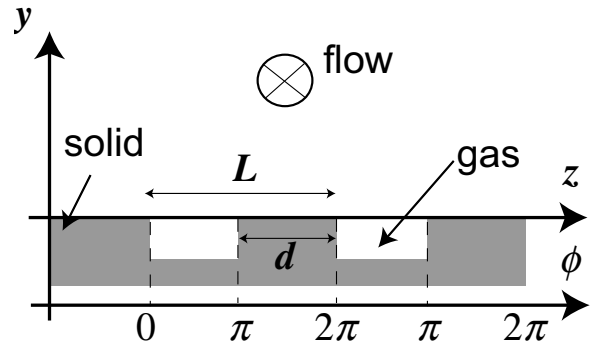


Figure 2. Schematic of flow over a hydrophobic surface and the phase ϕ with respect to the surface structure. The solid fraction is given by $\Phi = d/L$

resolution of $\Delta x = 11.0$ in streamwise and $\Delta z = 2.2$ in spanwise direction, while the minimum of the wall-normal grid spacing is $\Delta y_{min} = 0.1$. All statistics presented in the following are obtained for an integration time of $t = 10440$ with a time step of $\Delta t = 0.036$.

The geometry of the superhydrophobic surface is characterized by the periodicity L as shown in figure 2 and the solid fraction Φ which is defined as $\Phi = d/L$. The solid fraction Φ is kept constant at $\Phi = 0.5$ while the geometric wave-length, L , is varied in order to investigate the impact of groove width on the drag reduction effect. In comparison to the no-slip wall the superhydrophobic surface leads to an increase of the bulk flow rate. In contrast, for laminar flow conditions this change of the bulk flow rate is defined exclusively through the resulting average slip velocity at the wall, u_s , which can be linked to l_s in accordance with Eq. (1). The effective slip length can be predicted analytically for laminar flow conditions (Philip, 1972) and is obtained as a result of the DNS in turbulent flows.

DECOMPOSITION OF VELOCITY FIELD

Due to the periodically varying boundary condition in spanwise direction, it is likely that the statistical features of the turbulent velocity field show a similar periodicity. Ac-

Accordingly, a phase averaging operator leading to a triple decomposition is introduced as

$$\langle f \rangle(\phi, y) = \frac{1}{N} \sum_{n=1}^N \int_t \int_x f \left(x, y, L \left(\frac{\phi}{2\pi} + n \right), t \right) dx dt, \quad (4)$$

where f is an arbitrary variable and a function of space and time, while ϕ is a phase with respect to the periodic structure as shown in figure 2 and N is a number of periods in the computational domain. Averaging $\langle f \rangle$ over ϕ results in the spatial mean:

$$\bar{f}(y) = \frac{1}{2\pi} \int_0^{2\pi} \langle f \rangle(\phi, y) d\phi. \quad (5)$$

Accordingly, coherent fluctuations are defined as

$$\tilde{f}(\phi, y) = \langle f \rangle(\phi, y) - \bar{f}(y). \quad (6)$$

Thus, any flow quantity can be decomposed as follows:

$$\begin{aligned} f(x, y, z, t) &= \langle f \rangle(\phi, y) + f''(x, y, z, t) \\ &= \bar{f}(y) + \tilde{f}(\phi, y) + f''(x, y, z, t), \end{aligned} \quad (7)$$

where a quantity with a double prime represent the deviation from the phase average, and is referred to as random fluctuation throughout this paper. We also define the overall fluctuation as the deviation from the spatial mean:

$$\begin{aligned} f'(x, y, z, t) &= f(x, y, z, t) - \bar{f}(y) \\ &= \tilde{f}(y, \phi) + f''(x, y, z, t). \end{aligned} \quad (8)$$

This is equivalent to the definition of a fluctuating component in the conventional Reynolds averaging for no-slip walls with a homogeneous spanwise direction. In the case of the hydrophobic surface with streamwise grooves, the overall fluctuations are given by a sum of coherent and random fluctuations as shown in (8). Accordingly, the correlation of two arbitrary quantities f and g can be obtained as

$$\overline{f'g'} = \overline{\tilde{f}\tilde{g}} + \overline{f''g''}. \quad (9)$$

RESULTS

Increase in Flow Rate

In general, the presence of a superhydrophobic surface with streamwise grooves increases the bulk mean velocity compared to a turbulent channel flow with no-slip walls at the same friction Reynolds number and constant channel height. In figure 3 the corresponding gain in flow rate is plotted as a function of the different geometric wave-length, L , of the grooved surface structure. The gain strongly increases with increasing L initially but levels off for values above $L \approx 100$. For the biggest L considered, even a slight decrease in the resulting flow rate is observed compared to the second largest wave-length. This apparent limit of the achievable increase of flow rate is particular for turbulent

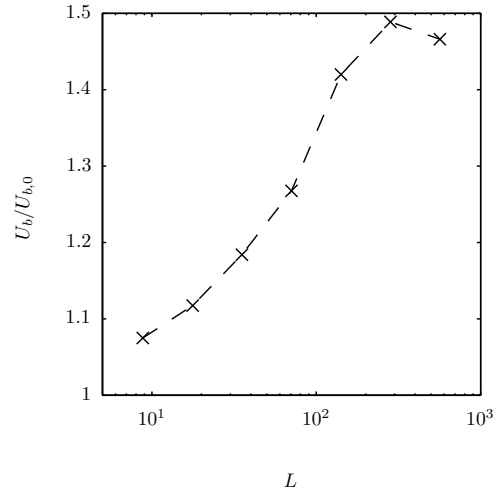


Figure 3. Gain in terms of an increase in U_b compared to the smooth reference channel

flows, since for laminar flow conditions the effective slip length is proportional to L as (Philip,1972)

$$\frac{L_s^*}{L^*} = \frac{-1}{\pi} \log \left[\cos \left\{ \frac{\pi}{2} (1 - \Phi) \right\} \right] \quad (10)$$

Velocity Statistics over Superhydrophobic Surface

Mean Velocity Profile The reason for the upper limit in the achievable flow rate becomes visible when the velocity profiles for different L are analyzed. These are shown in figure 4. The general shape of the velocity profile found above the superhydrophobic walls is maintained with an offset at the wall that corresponds to the slip velocity. If the profiles are corrected by this offset they collapse within the viscous sublayer (as expected for DNS with constant pressure gradient). In the channel center, however, the relative velocity decreases with increasing L indicating additional turbulent losses. This trend is in agreement with the results for a spatially uniform slip length (Min et al. 2004, Fukagata et al. 2006) where it is found that spanwise slip leads to an enhancement of turbulence, and thus reduces the positive effect of streamwise slip conditions.

Reynolds Stresses The normal components of the Reynolds stress tensor are shown in figures 5 through 8 following the decomposition defined in Eq. (7). The coherent contribution to the normal stresses is naturally largest for the streamwise component, for which $\overline{u'^2}$ increases with increasing L . This increase is due to the fact that higher velocities can develop along a wider groove, i.e. a free-slip surface. The coherent component of the streamwise velocity fluctuations decreases with increasing wall distance. The periodic contributions to $\overline{v'^2}$ and $\overline{w'^2}$ are negligibly small for small L but increase for the two largest wave-lengths, suggesting the presence of a secondary flow. This observation will be discussed in more detail later.

The random contributions to the normal stresses qualitatively show the same trends as the ones for flows over no-slip walls. Non-zero values of u''^2 and w''^2 at the wall arise from the no-shear condition while v''^2 has to approach

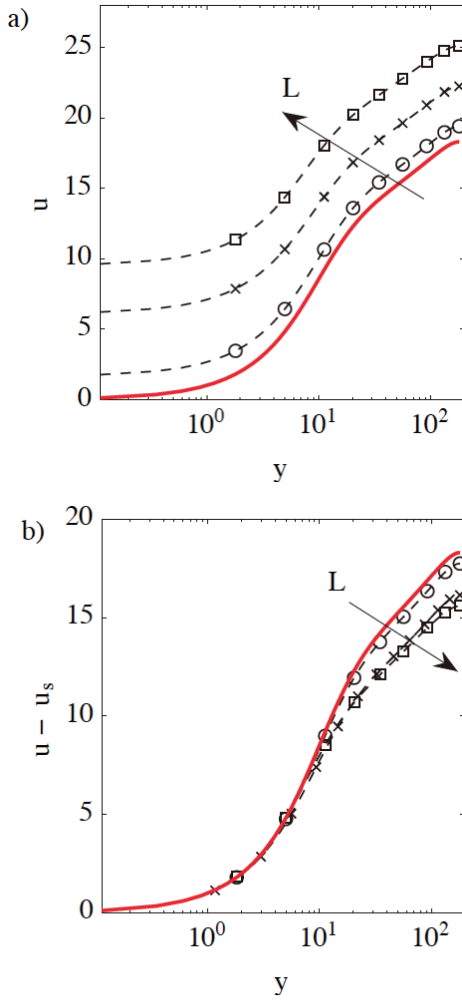


Figure 4. Mean velocity profile a) with and b) without slip velocity. thick solid line: solid wall, broken line with symbols: superhydrophobic surface. circle: $L = 35.2$, diamond: $L = 70.4$, up-pointing triangle: $L = 140.8$, down-pointing triangle: $L = 281.6$, right-pointing triangle: $L = 563.2$

zero due to non-permeability of the boundary. In general an increase of the peak value and a slight shift of its location towards smaller wall distances can be observed. Min et al. (2004) report decreasing peak values of the normal stresses for combined streamwise and spanwise slip. This difference is most likely caused by the different simulation strategies: the pressure gradient is fixed in the present work while Min et al. (2004) run DNS at constant flow rate. Therefore, the power input into the flow (i.e., the product of flow rate and pressure gradient) changes in the opposite direction when drag reducing superhydrophobic surfaces are introduced. It decreases for constant flow rate while it increases for constant pressure gradient. The decrease or increase in the normal Reynolds stresses reflects this modification of the energy injection rate into the flow.

The Reynolds shear stresses for different wave lengths are plotted in figure 8. The total shear stress generally increases with increasing L (which is consistent with the observed decrease of the relative mean velocity in figure 4 b)). However, a saturation of this effect can be observed. The coherent contribution, which indicates the presence of a secondary flow structure, is relatively smaller than the random

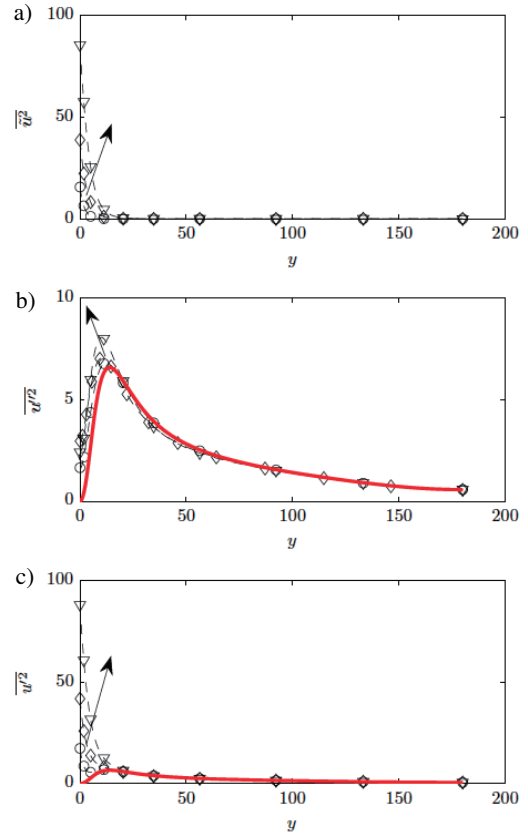


Figure 5. Variance of streamwise velocity fluctuation a) coherent, b) random components and c) their sum. The notations of lines and symbols are the same as those in figure 4.

one but shows the interesting fact of a reversed sign for the two largest wave-lengths: negative values of $-\overline{u''v''}$ are observed for these configurations.

Secondary Flow

Secondary flow structures of Prandtl's second kind, i.e. in the form of streamwise vortices, are observed for a geometric wave length of $L \geq 70.4$ in the present investigation. Figure 9 shows the contour of the phase averaged streamwise velocity profile along with streamlines for the phase-averaged in-plane velocities for two different L . For a wave length of $L = 140.8$ a counter-rotating secondary flow structure is clearly visible which extends roughly one wave-length in wall-normal direction. To our knowledge, the formation of such secondary flow structures over superhydrophobic surfaces has not been reported before. However, it is known from Goldstein et al. (1998) that similar secondary flows occur in turbulent flow over riblets if a certain riblet spacing is exceeded.

In order to further investigate the mechanism and the dynamics of the secondary flow, we consider the transport equation for the phase averaged streamwise vorticity $\langle \omega_x \rangle$:

$$\begin{aligned} & \langle v \rangle \frac{\partial \langle \omega_x \rangle}{\partial y} + \langle w \rangle \frac{\partial \langle \omega_x \rangle}{\partial z} \\ &= -\frac{\partial^2 \langle w''v'' \rangle}{\partial y^2} - \frac{\partial^2 \langle w''w'' \rangle}{\partial y \partial z} + \frac{\partial^2 \langle v''v'' \rangle}{\partial y \partial z} + \frac{\partial^2 \langle v''w'' \rangle}{\partial z^2} \\ &+ \frac{1}{Re_\tau} \left(\frac{\partial^2 \langle \omega_x \rangle}{\partial y^2} + \frac{\partial^2 \langle \omega_x \rangle}{\partial z^2} \right). \end{aligned} \quad (11)$$

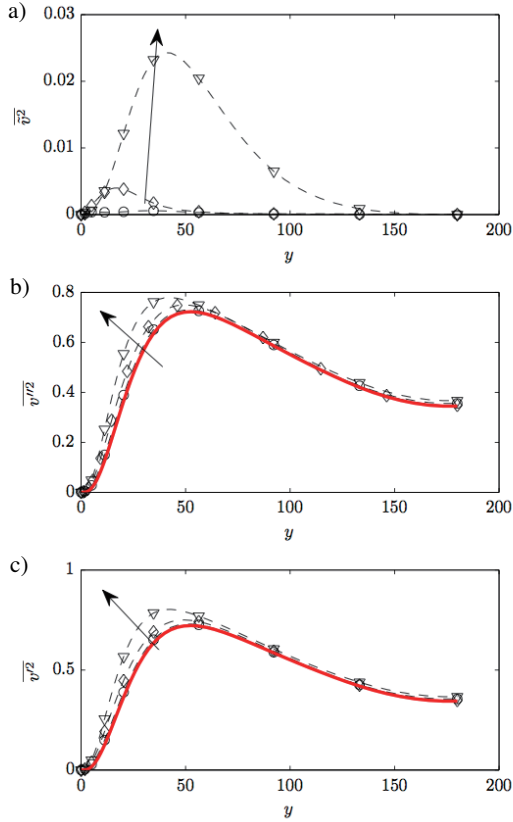


Figure 6. Variance of wall-normal velocity fluctuation a) coherent, b) random components and c) their sum. The notations of lines and symbols are the same as those in figure 4.

The terms on the left-hand-side represent the convection of $\langle \omega_x \rangle$ due to the secondary flow. The first four terms on the right-hand-side are production terms of $\langle \omega_x \rangle$, while the last term represents the viscous diffusion of $\langle \omega_x \rangle$. Note that the production terms have non-zero values only when the no-slip and no-shear surfaces are resolved. Therefore, the effective slip model introduced by Min et al. (2004) and Fukagata et al. (2006), which is homogeneous in the spanwise direction, does not lead to the formation of secondary flow.

Figure 10 shows the distribution of $\langle \omega_x \rangle$ and also the sum of the four production terms of Eq. (11) for the groove widths $L = 70.4$ and $L = 281.6$. For $L = 70.4$, the phase averaged flow moves towards the boundary in the middle of the free-slip region, and moves away from the wall in the middle of the no-slip region (see, figure 10 a)). In figure. 10 b), the distribution of $\langle \omega_x \rangle$ agrees quite well with the locations where $\langle \omega_x \rangle$ is produced according to Eq. (11), indicating that the inhomogeneity of the Reynolds stress is the primary reason for the generation of the secondary flow. We note that $-\partial^2 \langle w''v'' \rangle / \partial y^2$ is dominant among the four production terms of $\langle \omega_x \rangle$: it is almost two orders of magnitude larger than the other terms. For the groove width $L = 281.6$, a vortical structure can be observed which is located further away from the wall and possesses the opposite rotational direction (see, figure. 10 c)). Namely, a downwelling motion occurs over the no-slip area, while the upwelling is located above the free-slip area. This reversed vorticity leads to the change of sign for the coherent part of the Reynolds shear stress as observed in figure 8.

While the secondary motion is significantly differ-

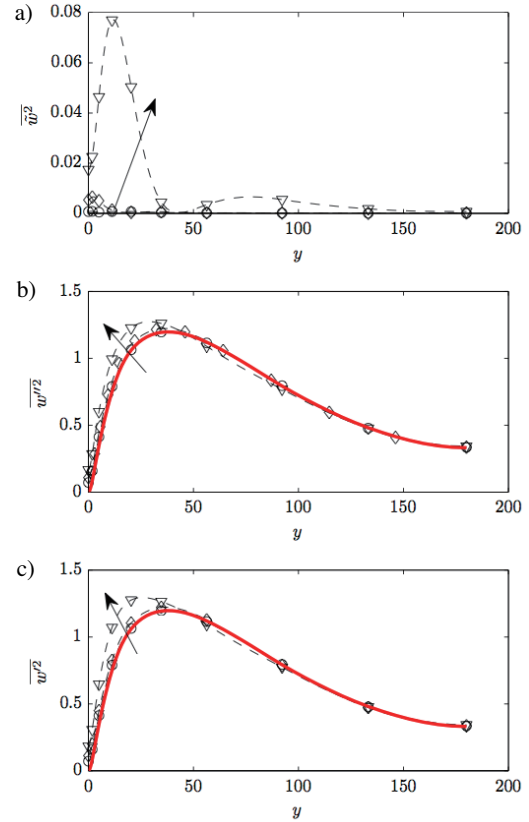


Figure 7. Variance of spanwise velocity fluctuation a) coherent, b) random components and c) their sum. The notations of lines and symbols are the same as those in figure 4.

ent for the two L considered, the distribution of the production term is nearly unchanged by L as shown in figures 10 b) and d). In both cases it is mainly determined by $-\partial^2 \langle w''v'' \rangle / \partial y^2$. The absolute value of the production term is largest close to the boundary between free-slip and no-slip regions. Its spatial extent in the spanwise direction is around $\Delta z \approx 30$ and almost independent of L . For $L = 70.4$ the two neighboring secondary vortices with opposite sign force the flow upward above the no-slip area and downward over the free-slip region. For $L = 281.6$ the same production mechanism acts at the interface between the no-slip and the free-slip wall. In this case, however, the extension of the locally induced vortices (which can be seen in figure 10c) is much smaller than their spanwise separation. Thus they do not interact directly but induce an additional vortical motion at larger wall distance as illustrated in figure 11.

CONCLUSIONS

DNS of turbulent flows over superhydrophobic surfaces where the surface structure of streamwise oriented grooves is modeled as an alternating no-slip and no-shear boundary conditions in the spanwise direction show the occurrence of secondary flow structures. Interestingly, the rotation direction of the secondary vortices becomes reversed once the spanwise period of superhydrophobic surface is above $L \approx 70$ in the friction unit. This causes a considerable change in the Reynolds shear stress, so that affects the resultant increase in the bulk mean velocity. The present results indicate that the precise modeling of turbulent dynam-

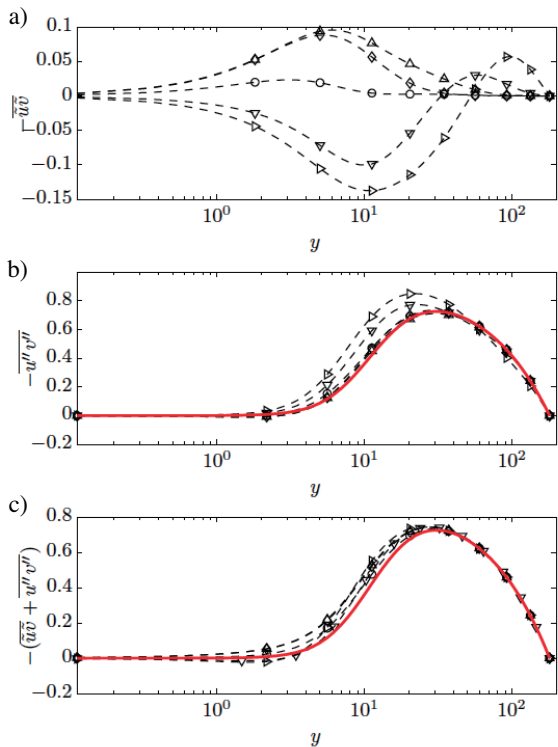


Figure 8. Reynolds shear stress profile a) coherent, b) random components and c) their sum. The notations of lines and symbols are the same as those in figure 4.

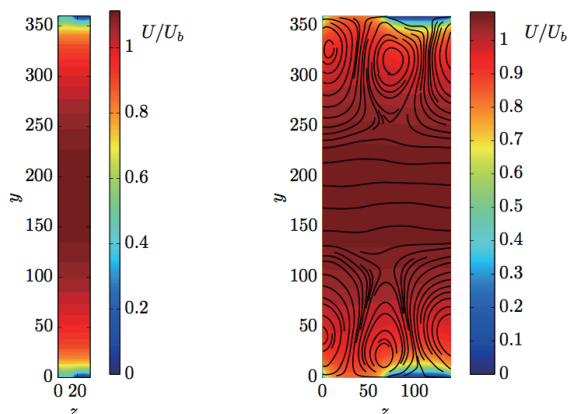


Figure 9. Contour of phase averaged streamwise velocity normalized with U_b including streamlines in the y - z -plane, left: $L = 35.2$, right: $L = 140.8$

ics over superhydrophobic surfaces is necessary in order to predict the drag reduction effect accurately.

REFERENCES

Busse, A. and Sandham, N. D., 2012, "Influence of an anisotropic slip-length boundary condition on turbulent channel flow", *Physics of Fluids*, Vol. 24, 055111.

Daniello, R. J., Waterhouse, N. E. and Rothstein, P., 2009, "Drag reduction in turbulent flows over superhydrophobic surfaces", *Physics of Fluids*, Vol. 21, 085103.

Fukagata, K., Kasagi, N. and Koumoutsakos, P., 2006, "A theoretical prediction of friction drag reduction in turbu-

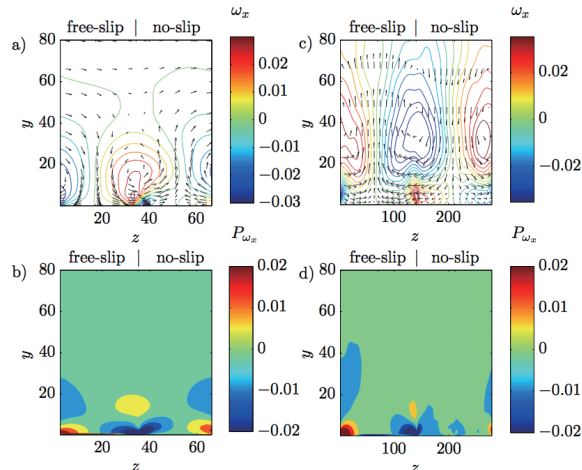
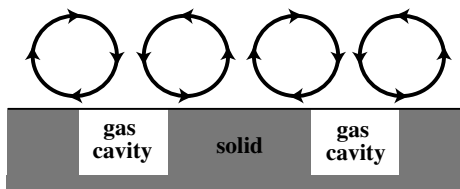


Figure 10. Secondary flow and a sum of the production term of $\langle \omega_x \rangle$. At $L = 70.4$: a) $\langle \omega_x \rangle$ and b) production of $\langle \omega_x \rangle$. At $L = 281.6$: c) $\langle \omega_x \rangle$ and d) production of $\langle \omega_x \rangle$

a)



b)

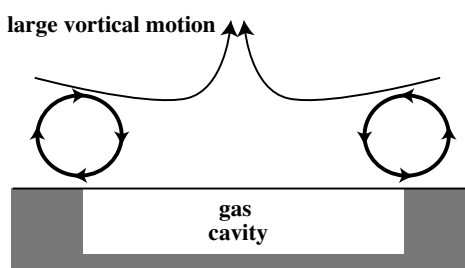


Figure 11. Mechanism of secondary flow over a superhydrophobic surface a) small and b) large groove width.

lent flow by superhydrophobic surfaces", *Physics of Fluids*, Vol.18, 051703-4.

Martell, M. B., Perot, J. B. and Rothstein, J. P., 2009, "Direct numerical simulation of turbulent flows over superhydrophobic surfaces", *Journal of Fluid Mechanics*, Vol. 620, pp. 31-41.

Min, T. and Kim, J., 2004, "Effects of hydrophobic surface on skin-friction drag", *Physics of Fluids*, Vol.16, L55.

Philip, J. R., 1972, "Flow satisfying mixed no-slip and no-shear conditions", *ZAMP*, Vol. 23, pp. 353-372.

Goldstein, D.B. and Tuan, T. C., 1998, "Secondary flow induced by riblets", *Journal of Fluid Mechanics*, Vol.363, pp.115-151.